Discovery of a hexagonal ultradense hydrous phase in (Fe,Al)OOH

Li Zhang[a,1], Hongsheng Yuan[a], Yue Meng[b], and Ho-kwang Mao[a,c,1]

[a]Center for High Pressure Science and Technology Advanced Research, 201203 Shanghai, China; [b]High Pressure Collaborative Access Team, Geophysical Laboratory, Carnegie Institution of Washington, Argonne, IL 60439; and [c]Geophysical Laboratory, Carnegie Institution of Washington, Washington, DC 20015

A deep lower-mantle (DLM) water reservoir depends on availability of hydrous minerals which can store and transport water into the DLM without dehydration. Recent discoveries found hydrous phases AlOOH (Z = 2) with a $CaCl_2$-type structure and FeOOH (Z = 4) with a cubic pyrite-type structure stable under the high-pressure–temperature (P-T) conditions of the DLM. Our experiments at 107–136 GPa and 2,400 K have further demonstrated that (Fe,Al)OOH is stabilized in a hexagonal lattice. By combining powder X-ray-diffraction techniques with multigrain indexation, we are able to determine this hexagonal hydrous phase with a = 10.5803(6) Å and c = 2.5897(3) Å at 110 GPa. Hexagonal (Fe,Al)OOH can transform to the cubic pyrite structure at low T with the same density. The hexagonal phase can be formed when δ-AlOOH incorporates FeOOH produced by reaction between water and Fe, which may store a substantial quantity of water in the DLM.

X-ray diffraction | hydrous mineral | lower mantle | deep-water cycle

Water enters the Earth's interior through hydrated subducting slabs (1). A hydrous mantle transition zone is indicated by the high water storage capacity of wadsleyite and ringwoodite (2, 3) and water can be further transported into the shallow lower mantle through dense hydrous phases (4, 5). Recent discoveries of several stable dense hydrous minerals at higher high-pressure–temperature (P-T) conditions have made deep-water cycle a hot topic. The phase H [$MgSiO_2(OH)_2$] (6) is isostructural to the δ-phase AlOOH, which adopts the $CaCl_2$-type structure above 8 GPa (7). Enrichment of AlOOH in the H-δ solid solution can stabilize the hydrous phase to higher P-T conditions (8). Both phase H and the δ-phase were elsewhere synthesized in a multianvil apparatus below 50 GPa, and the samples were examined by both in situ X-ray diffraction (XRD) under high P-T conditions and ex situ methods on the recovered samples (6, 9). Therefore, the structure and composition of the phase H and δ-phase are well understood, except that pressure effect on the hydrogen bond remains controversial (10, 11). On the other hand, both FeO_2 (12) and $FeOOH_x$ (13) [or FeOOH (14)] were recently discovered in a cubic pyrite-type structure (referred to as "Py phase") under P-T conditions of deep lower mantle (DLM). The structures were unquenchable to ambient conditions but a combination of theory and powder XRD data confirms the structure assignment beyond reasonable doubt (12, 14). Theoretical predictions indicate that the δ-phase AlOOH will eventually transform from the $CaCl_2$-type structure to the pyrite-type structure above 170 GPa (15), indicating that the high-P phase adopts the cubic pyrite-type structure.

Identification of hydrous phases in the lower-mantle system can provide essential information for understanding the deep-water cycle. There exist some data from phase-equilibria studies in a water-bearing but Fe-free lower-mantle composition where the Al-rich H-δ phase was the stable hydrous phase under the DLM P-T conditions above 50 GPa (8, 16). The δ-H solid solution $AlOOH$-$MgSiO_2(OH)_2$ approaches the AlOOH endmember at increasing P-T conditions, and coexists with Al-poor perovskite or postperovskite (8, 17). On the other hand, recent experiments identified the formation of Py-phase FeOOH from reactions of

water with iron in a wide range of oxidation states, from Fe to Fe_2O_3, under DLM high P-T conditions (18). Then, is the solid solution (Fe,Al)OOH stable when the δ-phase AlOOH incorporates the Py-phase FeOOH near the core-mantle boundary? In this study, we performed high P-T experiments to investigate (Fe,Al)OOH in a laser-heated diamond anvil cell (DAC) at 16-ID-B of the Advanced Photon Source (APS). Surprisingly, we discovered a very dense Fe-rich hydrous phase in (Fe,Al)OOH but it exhibits in a hexagonal lattice under high P-T conditions of DLM. The hexagonal phase converts to the cubic Py phase at low T with the same density.

Experimental Observations and Sample Characterization

The H_2O-bearing gel starting materials were prepared in two different compositions with molar rations of Fe_2O_3: Al_2O_3 of 3:2 and 4:1, denoted as A40 and A20, respectively. The experiments were conducted at 110 GPa and 2,200–2,400 K on the A40 sample, quenched to room temperature, and the XRD patterns were collected in situ under high P-T conditions, and after T quench (Fig. 1 and Table 1). The Py phase was absent in A40, but we observed a hexagonal phase (denoted as "HH phase") coexisting with the δ-phase AlOOH (19). Seven powder XRD peaks roughly constrained a hexagonal lattice with a = b = 10.59(3) Å, c = 2.586(5) Å, and V = 251.3(8) and the coexisting orthorhombic δ-phase has a unit cell of a = 4.273(1) Å, b = 3.838(1) Å, c = 2.546(1) Å, and V = 41.75(2) Å^3 (Table 1). The lattice volume of the δ-phase is in good agreement with the extrapolated equation of state of the δ-phase AlOOH (20). The lattice volume of the HH phase is six times of that of δ-phase (Z = 2) (*SI Appendix*, Table S1).

Significance

The lower mantle is potentially the most massive water reservoir in our planet, which largely depends on availability of hydrous minerals which can store and transport water down to the deep lower mantle. Experimentally, it is a great challenge to identify an unknown hydrous phase in a multiphase system under high-pressure–temperature conditions corresponding to the deep Earth. We combined powder X-ray diffraction and multigrain indexation to discover a hexagonal hydrous phase in (Fe,Al)OOH at 107–136 GPa and 2,400 K. Tens of individual crystallites, each with its unique orientation matrix, confirm the existence of the hexagonal phase. This study highlights a candidate for water storage.

Fig. 1. Powder XRD pattern of the HH phase and coexisting δ-phase in A40. The HH phase (marked with red dots) was found coexisting with the δ-phase AlOOH at 2,200–2,400 K as well as after *T* quench at 110 GPa (X-ray wavelength: 0.3445 Å). The calculated peak positions of the HH phase and δ-phase are indicated by small ticks. The diffraction peaks of Re were originated from the gasket.

Table 1. Indexed powder XRD peaks of the HH phase and coexisting δ-phase in A40

Phase	hkl	2θ-obs, °	d-obs, Å	d-calc, Å	d-diff, Å
HH	400	8.629	2.2899	2.2939	−0.0040
	211	9.527	2.0745	2.0731	0.0014
	221	10.684	1.8504	1.8503	0.0000
	311	10.900	1.8138	1.8138	0.0000
	321	12.121	1.6317	1.6325	−0.0008
	421	13.727	1.4415	1.4402	0.0013
	402	17.593	1.1265	1.1264	0.0001
δ	110	6.919	2.8548	2.8556	−0.0007
	111	10.396	1.9015	1.9005	0.0009
	121	13.720	1.4423	1.4426	−0.0004
	220	13.855	1.4283	1.4278	0.0005
	002	15.553	1.2732	1.2732	0.0000
	301	15.931	1.2431	1.2432	−0.0001
	331	22.282	0.8916	0.8916	−0.0001

The HH phase has a hexagonal symmetry and its lattice parameters are $a = b = 10.59(3)$ Å, $c = 2.586(5)$ Å, and $V = 251.3(8)$ Å^3 and the lattice parameters of the orthorhombic δ-phase are $a = 4.273(1)$ Å, $b = 3.838(1)$ Å, $c = 2.546(1)$ Å, and $V = 41.75(2)$ Å^3 at 110 GPa and after *T* quench. The integrated powder XRD pattern is shown in Fig. 1 ($\lambda = 0.3445$ Å).

Identification of an unknown phase in an environment of multiple crystals and multiple phases is a great challenge, especially under high *P-T* conditions. Fortunately the high degree of spottiness in the A40 experiment (*SI Appendix*, Fig. S2A) allowed the multigrain indexation (21, 22), which could provide single-crystal–like information for each individual crystal in the assemblage (23, 24). The multigrain dataset was collected by rotating the ω-(vertical) axis of the DAC to ±23° at the steps of 0.25°. The *d* spacings of those unidentified peaks in the powder XRD pattern suggested several possible lattices. Then each lattice was used as an input for grain indexation and only the hexagonal lattice was confirmed by finding 27 individual crystallites, each with 50–120 reflections consistent with the input lattice. *SI Appendix*, Table S2 shows an example of 104 reflections originating from one of the selected crystallites. Each reflection has three variables (ω, η, and 2θ) to constrain the orientation matrix, where ω, η, and θ represent the rotation, azimuth, and Bragg angles, respectively, with the total of 312 variables confirming the lattice of the HH phase. Moreover, 27 individual crystallites, each with its particular orientation matrix, redundantly confirmed the same HH lattice. An example demonstrating six symmetry-equivalent reflections of {311} at $d = 1.815$ Å belonging to one crystallite of the HH phase is shown in Fig. 2. The multigrain method also has the advantage of picking out weak reflection spots, such as the 110 and 220, which are too weak to show as a peak after 2D integration of powder ring, but stand out as individual single spots. Reflections from one selected crystallite of the coexisting δ-phase are also listed in *SI Appendix*, Table S3.

The decomposition of A40 into the δ-AlOOH and HH phase indicates that the Al content in the HH phase is considerably less than 40%. To constrain the Al content in the HH phase and to search for the possible Py phase of the solid solution (Fe,Al)OOH, we conducted a similar high *P-T* experiment on the A20 sample. Fig. 3 shows the XRD pattern collected at 107 GPa and after *T* quench in the center of heated spot (denoted as *C* region) which was originally pressurized to 101 GPa, heated to 2,200–2,400 K, quenched to room temperature, and pressure increased to 107 GPa after the *T* quench. The strong peaks all belong to the HH phase, coexisting with small amounts of the Py phase. The indexed diffraction peaks are consistent with the HH phase with $a = b = 10.588(4)$ Å, $c = 2.596(1)$ Å, and $V = 252.1(1)$ Å^3 at 107.0 GPa and after *T* quench, and the weak peaks of the Py phase are consistent with $a = 4.3821(4)$ Å (Table 2). Very little δ-AlOOH is present, indicating that the composition is close to the Al limit in the hexagonal (Fe,Al)OOH.

Through an XRD 2D scan at steps of 5 μm, a larger proportion of the cubic Py phase was observed coexisting with the HH phase at the rim position (*R* region), 10 μm from the center. The *R* region

was at the slope of the laser heating spot and thus was subjected to lower temperature and higher Fe content than the *C* region according to the chemical migration caused by the Soret diffusion (25). The Al content is higher than A20 [Al/(Al+Fe) > 20 mol %] in the *C* region and lower than A20 in the *R* region to balance the A20 bulk composition. We obtained the lattice parameters of $a = 4.3836(5)$ Å and $V = 84.23(1)$ Å^3 for the Py phase
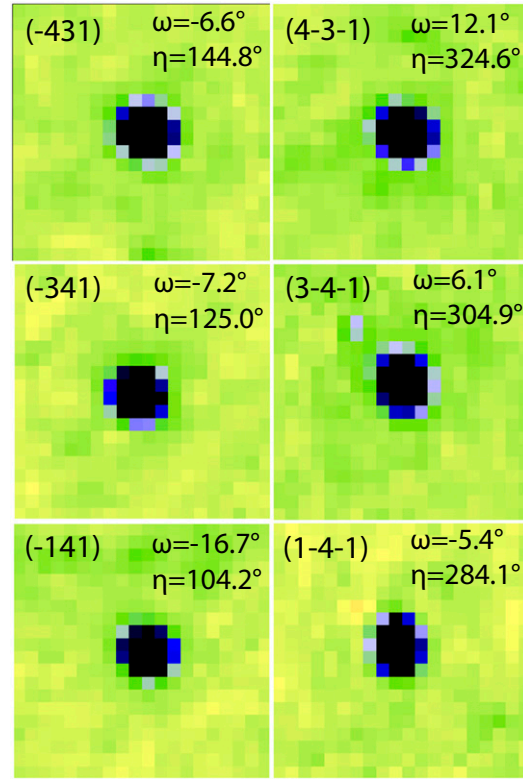

Fig. 2. A selected crystallite of the HH phase. Six symmetry-equivalent reflections at $d = 1.815$ Å from the selected crystallite of the HH phase (Fe,Al)OOH at 110 GPa.
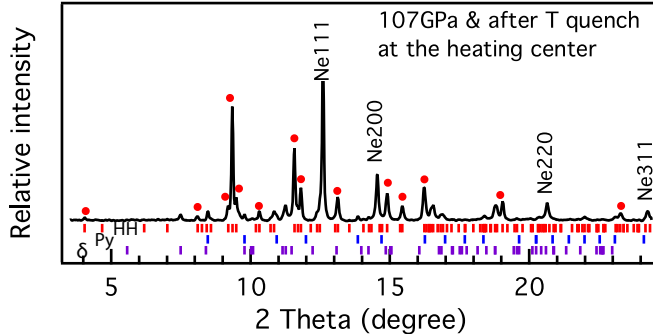
Fig. 3. Powder XRD pattern of the HH phase in A20 collected in region C. The HH phase (marked with red dots) was dominant under *P-T* conditions of 107.0 GPa and 2,000–2,400 K (X-ray wavelength: 0.3738 Å). The calculated peak positions of the HH phase, Py phase, and δ-phase are indicated by small ticks, showing coexistence of small amount of both P-phase and δ-phase.

and $a = b = 10.598(11)$ Å, $c = 2.599(2)$ Å, and $V = 252.8(3)$ Å^3 for the HH phase in the *R* region at a slightly higher pressure of 107.8 GPa (*SI Appendix*, Table S1). We noticed that the expected volume per formula (*V/Z*) of the HH phase ($z = 12$) is again equal to that of the Py phase ($z = 4$) within the experimental uncertainties (*SI Appendix*, Table S1).

Interestingly, the *C* and *R* regions behave differently upon reheating due to the small difference in Al/(Al+Fe) ratio. In the *R* region where the HH phase coexisted with the Py phase with comparable diffraction peak intensities, the Py phase transformed to the nearly pure HH phase after heating at 2,000 K for only 4 min (Fig. 4*A*), an indication of the Py phase being a low-*T* polymorph of the HH phase. The HH phase remained as the dominant phase immediately after *T* quench (Fig. 4*B*) but then we observed a gradual growth of the Py phase at the expense of the HH phase with increasing time while the sample remained at room temperature. After 25 min from *T* quench, the HH phase and Py phase regained their preheating proportion, which remained stable afterward (Fig. 4*C*). The conversion process between the HH phase and Py phase was repeatable. In contrast, the central region *C* remained dominated by the HH phase during reheating and after *T* quench (Fig. 3), indicating that increasing Al content stabilizes the HH phase at low *T*, which was also confirmed by the absence of the Py phase in A40. The Al content in the HH phase was much less than A40 (Fig. 1) and very close to A20 (Fig. 3), thus estimated as $(Fe_{0.8}Al_{0.2})OOH$. The Py phase with slightly more Fe than A20 is only stable at low *T* whereas the Py-phase FeOOH was found stable at least to 2,500 K (13, 14). These combined, suggesting that the stability of the Py phase expands to high *T* as its composition approaches the FeOOH endmember.

Discussions and Geophysical Implications

We note that the coexisting HH phase, Py phase, and δ-AlOOH in this study all have nearly identical volumes per formula within the experimental uncertainties (*SI Appendix*, Table S1). The lattice parameters of the HH phase ($Z = 12$) and the coexisting δ-phase ($Z = 2$) were determined from the single crystals selected by the multigrain method (*SI Appendix*, Tables S2 and S3). The ionic radius of Fe^{3+} is reduced to the comparable size of Al^{3+} after a high-spin to low-spin transition above 50 GPa (26) so that increasing Fe/Al ratio may only slightly increase the volumes of the hydrous phases. The volume of the most hydrous $FeOOH_x$ expands ~8% relative to that of FeO_2 in the Py phase at 110 GPa (13) and the volumes of both the HH phase and coexisting Py phase are in good agreement with those of the most hydrous Py-$FeOOH_x$ (13, 14), indicating that the HH phase is hydrous.

This discovered hexagonal phase (Fe,Al)OOH is stable under the DLM conditions. We attempted to understand the structure

Table 2. Indexed powder XRD peaks of the HH phase and coexisting Py phase in A20

Phase	hkl	2θ-obs, °	d-obs, Å	d-calc, Å	d-diff, Å
HH	110	4.047	5.2932	5.2941	−0.0009
	220	8.094	2.6483	2.6470	0.0012
	111	9.199	2.3307	2.3311	−0.0004
	400	9.346	2.2941	2.2924	0.0017
	201	9.482	2.2613	2.2593	0.0020
	211	10.318	2.0785	2.0779	0.0006
	221	11.572	1.8539	1.8536	0.0004
	311	11.809	1.8168	1.8168	0.0000
	321	13.129	1.6349	1.6345	0.0004
	421	14.903	1.4412	1.4413	−0.0002
	511	15.447	1.3907	1.3907	0.0000
	440	16.234	1.3237	1.3235	0.0002
	402	19.047	1.1296	1.1296	0.0000
	442	23.277	0.9265	0.9268	−0.0003
Py	111	8.472	2.5303	2.5300	0.0003
	200	9.787	2.1910	2.1910	−0.0001
	220	13.858	1.5492	1.5493	−0.0001

The lattice parameters are $a = b = 10.588(4)$ Å, $c = 2.596(1)$ Å, and $V = 252.1(1)$ Å^3 for the HH phase and $a = 4.3821(4)$ Å and $V = 84.15(1)$ Å^3 for the coexisting weak Py phase at 107.0 GPa and after *T* quench. The integrated powder XRD pattern is shown in Fig. 3 ($\lambda = 0.3738$ Å).

details and found that several complications prevented us from obtaining a structure model. Firstly, it is challenging to determine the Fe/Al occupancy and we cannot rule out the presence of some vacancies in the structure. Secondly, possible existence of mixed
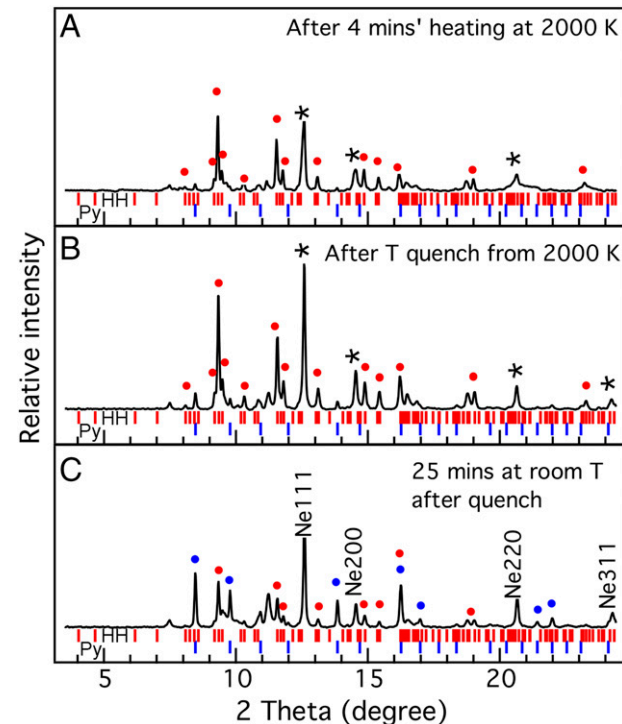
Fig. 4. Powder XRD patterns of the coexisting Py phase and HH phase in A20 collected in region *R*. The conversion between the Py phase and the HH phase upon reheating at 107.8 GPa (*P* measured after *T* quench): (*A*) the nearly pure HH phase (marked with red dots) after reheating at 2,000 K for 4 min; (*B*) after *T* quench; (*C*) gradual conversion from the HH phase to the Py phase (marked with blue dots) after 25 min at room temperature after quench (X-ray wavelength: 0.3738 Å). The peaks marked with stars belong to the Ne pressure medium.

valence states of Fe further complicates the structure (27). Last, we are not able to determine where and how hydrogen is located. The phase relations between the HH phase and Py phase determined its hydrous nature and constrained its composition but the exact H content in the HH phase is uncertain because only about half of the HH phase converted to the hydrous Py phase at room temperature (Fig. 4C). HH phase can be produced when δ-AlOOH in the subducting slabs incorporates FeOOH under the DLM conditions. Subducting along with the continuous slab penetration, the HH phase might accumulate at the bottom of the lower mantle due to its ultrahigh density. Measurements of sound velocities suggested that the V_S of δ-AlOOH is ~7% lower than that of magnesium silicate perovskite under DLM conditions (17) and the iron-rich (Fe,Al)OOH with high mean atomic numbers would be expected to have considerably lower V_S than δ-AlOOH. Indeed, recent measurements for $FeOOH_x$ in the pyrite-type structure showed dramatic velocity reductions in V_P and V_S, ~20% and 42%, respectively, relative to the seismic model values (28), providing an explanation for the origin of the ultralow-velocity zones (29). Our results showed that the HH phase is the high-temperature phase to the Py phase in the presence of Al, and Al indeed dominantly partitions into the hydrous phase rather than coexisting silicates at increasing *P-T* conditions (8, 17), so formation of the HH phase is expected in the DLM.

Methods

The gel was synthesized using a sol–gel method (30) from citric acid $C_6H_8O_7$, aluminum nitrate hydrate, and iron (III) nitrate hydrate. The high-purity powdered sample of aluminum nitrate hydrate, and iron (III) nitrate hydrate were weighed with molar rations of Fe_2O_3: Al_2O_3 = 3:2 and 4:1, respectively, and the corresponding gel samples were denoted as A40 and A20. The gel samples were dried at 650 or 700 °C to remove some amount of water in the starting materials (8). Energy dispersive spectroscopy mapping revealed a homogeneous starting material and the Fe/Al ratio remained unchanged after the synthesis (*SI Appendix*, Fig. S1). A piece of the gel sample was precompressed to ~10 μm thick and cut to ~50 μm in diameter and then placed in a Re recessed gasket hole of ~30-μm thickness. The sample disk was sandwiched between symmetric Ne layers before sealed. We brought the sample to the pressure of interest and heated it by the double-sided laser system at 16-ID-B of the APS (31). The incident monochromatic X-ray beam with energy of 30 or 36 KeV was focused to a size of ~5 × 5 μm² and the heating spot size was ~35 μm in diameter. Heating center, X-ray beam, and temperature measurement positions were aligned during the whole experiment (31). The heating temperature was determined by fitting Planck radiation function to the black-body radiation curve on both sides of the heating sample. Pressure was determined before and after heating based on the Ne pressure scale (32). The multigrain dataset was collected on a rotation stage using an X-ray beam with a wavelength of 0.3445 Å, recorded on a MarCCD detector. The sample-to-detector distance was calibrated using an XRD pattern of standard CeO_2 reference sample. The distance was set no closer than 190 mm to insert heating mirrors for in situ heating treatment (31).

1. van Keken PE, Hacker BR, Syracuse EM, Abers GA (2011) Subduction factory: 4. Depth-dependent flux of H₂O from subducting slabs worldwide. *J Geophys Res* 116:B01401.
2. Kohlstedt DL, Keppler H, Rubie DC (1996) Solubility of water in the α, β and γ phases of (Mg,Fe)₂SiO₄. *Contrib Mineral Petrol* 123:345–357.
3. Pearson DG, et al. (2014) Hydrous mantle transition zone indicated by ringwoodite included within diamond. *Nature* 507:221–224.
4. Liu L-g (1987) Effects of H₂O on the phase behaviour of the forsterite–enstatite system at high pressures and temperatures and implications for the Earth. *Phys Earth Planet Inter* 49:142–167.
5. Pamato MG, et al. (2014) Lower-mantle water reservoir implied by the extreme stability of a hydrous aluminosilicate. *Nat Geosci* 8:75–79.
6. Nishi M, et al. (2014) Stability of hydrous silicate at high pressures and water transport to the deep lower mantle. *Nat Geosci* 7:224–227.
7. Kuribayashi T, Sano-Furukawa A, Nagase T (2013) Observation of pressure-induced phase transition of δ-AlOOH by using single-crystal synchrotron X-ray diffraction method. *Phys Chem Miner* 41:303–312.
8. Ohira I, et al. (2014) Stability of a hydrous δ-phase, AlOOH–MgSiO₂(OH)₂, and a mechanism for water transport into the base of lower mantle. *Earth Planet Sci Lett* 401:12–17.
9. Suzuki A, Ohtani E, Kamada T (2000) A new hydrous phase δ-AlOOH synthesized at 21 GPa and 1000 C. *Phys Chem Miner* 27:689–693.
10. Tsuchiya J, Tsuchiya T, Tsuneyuki S, Yamanaka T (2002) First principles calculation of a high-pressure hydrous phase, δ-AlOOH. *Geophys Res Lett* 29:1909.
11. Vanpeteghem CB, Sano A, Komatsu K, Ohtani E, Suzuki A (2007) Neutron diffraction study of aluminous hydroxide δ-AlOOD. *Phys Chem Miner* 34:657–661.
12. Hu Q, et al. (2016) FeO₂ and FeOOH under deep lower-mantle conditions and Earth's oxygen-hydrogen cycles. *Nature* 534:241–244.
13. Hu Q, et al. (2017) Dehydrogenation of goethite in Earth's deep lower mantle. *Proc Natl Acad Sci USA* 114:1498–1501.
14. Nishi M, Kuwayama Y, Tsuchiya J, Tsuchiya T (2017) The pyrite-type high-pressure form of FeOOH. *Nature* 547:205–208.
15. Tsuchiya J, Tsuchiya T (2011) First-principles prediction of a high-pressure hydrous phase of AlOOH. *Phys Rev B* 83:054115.
16. Walter MJ, et al. (2015) The stability of hydrous silicates in Earth's lower mantle: Experimental constraints from the systems MgO–SiO₂–H₂O and MgO–Al₂O₃–SiO₂–H₂O. *Chem Geol* 418:16–29.
17. Mashino I, Murakami M, Ohtani E (2016) Sound velocities of δ-AlOOH up to core-mantle boundary pressures with implications for the seismic anomalies in the deep mantle. *J Geophys Res Solid Earth* 121:595–609.
18. Mao H-K, et al. (2017) When water meets iron at Earth's core–mantle boundary. *Natl Sci Rev* 4:870–878.
19. Sano A, et al. (2008) Aluminous hydrous mineralδ-AlOOH as a carrier of hydrogen into the core-mantle boundary. *Geophys Res Lett* 35:L03303.
20. Sano-Furukawa A, et al. (2009) Change in compressibility of δ-AlOOH and δ-AlOOD at high pressure: A study of isotope effect and hydrogen-bond symmetrization. *Am Mineral* 94:1255–1261.
21. Sørensen HO, et al. (2012) Multigrain crystallography. *Z Kristallogr* 227:63–78.
22. Schmidt S (2014) GrainSpotter: A fast and robust polycrystalline indexing algorithm. *J Appl Crystallogr* 47:276–284.
23. Zhang L, et al. (2014) Disproportionation of (Mg,Fe)SiO₃ perovskite in Earth's deep lower mantle. *Science* 344:877–882.
24. Zhang L, et al. (2016) In-situ crystal structure determination of seifertite SiO₂ at 129 GPa: Studying a minor phase near Earth's core–mantle boundary. *Am Mineral* 101:231–234.
25. Sinmyo R, Hirose K (2010) The Soret diffusion in laser-heated diamond-anvil cell. *Phys Earth Planet Inter* 180:172–178.
26. Merlini M, et al. (2010) Fe³⁺ spin transition in CaFe₂O₄ at high pressure. *Am Mineral* 95:200–203.
27. Bykova E, et al. (2016) Structural complexity of simple Fe₂O₃ at high pressures and temperatures. *Nat Commun* 7:10661.
28. Liu J, et al. (2017) Hydrogen-bearing iron peroxide and the origin of ultralow-velocity zones. *Nature* 551:494–497.
29. Thorne MS, Garnero EJ (2004) Inferences on ultralow-velocity zone structure from a global analysis of SPdKS waves. *J Geophys Res Solid Earth* 109:B08301.
30. Hamilton DL, Henderson MB (1968) The preparation of silicate compositions by a gelling method. *Mineral Mag* 36:832–838.
31. Meng Y, Hrubiak R, Rod E, Boehler R, Shen G (2015) New developments in laser-heated diamond anvil cell with in situ synchrotron x-ray diffraction at High Pressure Collaborative Access Team. *Rev Sci Instrum* 86:072201.
32. Fei Y, et al. (2007) Toward an internally consistent pressure scale. *Proc Natl Acad Sci USA* 104:9182–9186.